Wright, Matthew A., Surta, T. Wesley, Evans, Jae A., Lim, Jungwoo, Jo, Hongil, Hawkins, Cara J., Bahri, Mounib, Daniels, Luke M., Chen, Ruiyong, Zanella, Marco and others (2024) *Accessing Mg-Ion Storage in V 2 PS 10 via Combined Cationic-Anionic Redox with Selective Bond Cleavage.* Angewandte Chemie International Edition . ISSN 1521-3773.

GDCh

Research Articles

Angewandte
Chemie
International Edition
www.angewandte.org

Accessing Mg-Ion Storage in V$_2$PS$_{10}$ via Combined Cationic-Anionic Redox with Selective Bond Cleavage

Matthew A. Wright, T. Wesley Surta, Jae A. Evans, Jungwoo Lim, Hongil Jo,
Cara J. Hawkins, Mounib Bahri, Luke M. Daniels, Ruiyong Chen, Marco Zanella,
Luciana G. Chagas, James Cookson, Paul Collier, Giannantonio Cibin, Alan V. Chadwick,
Matthew S. Dyer, Nigel D. Browning, John B. Claridge, Laurence J. Hardwick, and
Matthew J. Rosseinsky*

Abstract: Magnesium batteries attract interest as alternative energy-storage devices because of elemental abundance and potential for high energy density. Development is limited by the absence of suitable cathodes, associated with poor diffusion kinetics resulting from strong interactions between Mg^{2+} and the host structure. V$_2$PS$_{10}$ is reported as a positive electrode material for rechargeable magnesium batteries. Cyclable capacity of 100 mAh g^{-1} is achieved with fast Mg^{2+} diffusion of 7.2×10^{-11}–4×10^{-14} cm^{2}s^{-1}. The fast insertion mechanism results from combined cationic redox on the V site and anionic redox on the (S$_2$)$^{2-}$ site; enabled by reversible cleavage of S–S bonds, identified by X-ray photoelectron and X-ray absorption spectroscopy. Detailed structural characterisation with maximum entropy method analysis, supported by density functional theory and projected density of states analysis, reveals that the sulphur species involved in anion redox are not connected to the transition metal centres, spatially separating the two redox processes. This facilitates fast and reversible Mg insertion in which the nature of the redox process depends on the cation insertion site, creating a synergy between the occupancy of specific Mg sites and the location of the electrons transferred.

Introduction

Li-ion batteries are approaching their theoretical energy densities.[1,2] Performance limitations combined with scarcity of lithium contrasts with the increasing demand for versatile rechargeable batteries. As such, continued innovation in energy storage technologies featuring a range of metals beyond lithium is required. The high volumetric capacity of magnesium (3833 mAh cm^{-3}) compared to that of lithium (2046 mAh cm^{-3}) and sodium (1125 mAh cm^{-3}) is a result of the ionic bivalency and close ion-packing.[3,4] In application, near 100 % coulombic efficiency of magnesium plating/ stripping has been reported.[5] The high natural abundance of magnesium vs. lithium (20,900 ppm vs. 20.0 ppm) and its relatively low cost make magnesium battery technologies an appealing alternative to lithium for potential applications in grid-scale energy storage.[6–9] While the intrinsic characteristics of magnesium rank it as one of the most promising metal anodes, there is a lack of suitable cathode materials. This is due to kinetic limitations concerning Mg^{2+} insertion into cathode materials.[10] The study of host materials that allows previously unknown Mg^{2+} storage and intercalation chemistries is critical to advance the development of positive electrode materials for Mg-ion technology.

Despite the comparable ionic radii of Mg^{2+} and Li$^+$ (0.57 vs. 0.59 Å),[11] the higher charge density of the divalent

[*] M. A. Wright, Dr. T. W. Surta, J. A. Evans, Dr. J. Lim, Dr. H. Jo,
     C. J. Hawkins, Dr. L. M. Daniels, Dr. R. Chen, Dr. M. Zanella,
     Dr. M. S. Dyer, Dr. J. B. Claridge, Prof. L. J. Hardwick,
     Prof. M. J. Rosseinsky
     Department of Chemistry, University of Liverpool, L69 7ZD Liverpool, UK
     E-mail: m.j.rosseinsky@liv.ac.uk

     M. A. Wright, Dr. J. Lim, Prof. L. J. Hardwick
     Stephenson Institute for Renewable Energy, University of Liverpool, L69 7ZF Liverpool, UK

     Dr. M. Bahri, Prof. N. D. Browning
     Albert Crewe Centre, University of Liverpool, Research Technology Building, Elisabeth Street, Pembroke Place, L69 3GE Liverpool, UK

     Dr. L. G. Chagas, Dr. J. Cookson, Dr. P. Collier
     Johnson Matthey Technology Centre, Sonning Common, RG4 9NH Reading, UK

     Dr. G. Cibin
     Diamond Light Source, Harwell Science and Innovation Campus, OX11 0DE Didcot, UK

     Prof. A. V. Chadwick
     School of Physical Sciences, University of Kent, CT2 7NH Canterbury, UK

     Prof. N. D. Browning
     School of Engineering, Department of Mechanical, Materials and Aerospace Engineering, University of Liverpool, L69 3GH Liverpool, UK

Mg cation leads to increased electrostatic interactions with the anion framework of the host structure. This is why many lithium insertion materials are unsuitable for multivalent ion insertion: V_2O_5,[12] spinels and postspinels such as Ni_2O_4 and Mn_2O_4,[13,14] TiO_2,[14] olivine $FePO_4$,[14] and VPO_4F,[15] all demonstrate poor intercalation kinetics for Mg^{2+}.[16,17] The higher polarizability of sulphur gives better kinetic performance for transition metal sulphides over oxides,[18–22] and the most prominent sulphide magnesium cathode is Mo_6S_8 which retains a reversible capacity of 70 mAh g^{-1} with an average discharge potential of 1.1 V over 2000 cycles.[23] Conversion-type materials, such as CuS, NiS and $CoS_{0.89}$, offer large capacities, >200 mAh g^{-1}, but suffer from significant structural and volumetric changes to the detriment of diffusion rate and cyclability.[24,25]

Anionic redox of $(O_2)^{2-}$ species has been studied extensively for next-generation cathode materials, however sulphides attract greater interest as Mg^{2+} insertion cathodes because of higher reaction reversibility and enhanced kinetics resulting from the lower chemical hardness of S^{2-} compared to O^{2-}.[26–32] Despite the lower operating potentials vs. Mg^{2+}/Mg of sulphides relative to oxides,[33] the multi-electron processes facilitated through anionic redox of $(S_2)^{2-}$ with simultaneous cationic redox can offer capacity enhancement.[34,35]

TiS_3 and VS_4 have one-dimensional metal-sulphur chains, bound by van der Waals (vdW) forces, containing S–S bonds in $(S_2)^{2-}$ units coordinated to the metal centres. Both have been studied as magnesium cathodes.[36–40] Combined cationic and anionic redox processes, accessed via partially reversible cleavage of S–S bonds, yield second cycle capacities of 105 mAh g^{-1} (0.3 Mg^{2+} per formula unit, f.u.) and 150 mAh g^{-1} (0.48 Mg^{2+}/f.u.), in TiS_3 and VS_4 respectively, with excellent rate performance. However, S–S bond cleavage within the chains produces metastable phases that undergo simultaneous and irreversible conversion-reactions producing MgS, TiS_2 and V metal. Significant capacity decay is observed within the first five cycles for both TiS_3 and VS_4.[41]

The structure of V_2PS_{10} is also one-dimensional, but built from phosphorous-containing $[P_2V_4S_{20}]_\infty$ chains along the [100] direction (Figure S1). These infinite chains are formed from biprismatic bicapped $[V_2S_{12}]$ units containing $[VS_8]$ environments that share a distorted rectangular face. Pairs of chains are covalently connected by $[P_2S_8]$ bitetrahedral groups, in which a $[PS_4]$ unit from each chain is bridged by a $(S_2)^{2-}$ bond. These $[P_2S_8]$ units covalently connect the chains, distinguishing V_2PS_{10} from TiS_3 and VS_4 where only vdW forces connect the chains. The bridging $(S_2)^{2-}$ bond is not the only disulphide in the structure of V_2PS_{10}, as each $[VS_8]$ unit is formed by three discrete $(S_2)^{2-}$ anions that are coordinated directly to the metal centre, together with two S^{2-} anions that also form the PS_4 unit.[42] Due to the presence of the two chemically distinct and spatially separated types of $(S_2)^{2-}$ anion, the electrochemical activity of the S–S bond that bridges the two P^{5+} centres is expected to differ from that of those coordinated to V. The oxidation states in V_2PS_{10} can be considered through the structural motif that contains one of these bridging S–S bonds; $V_2^{4+}+P_2^{5+}$

$(S_2)^{2-}_7S^{2-}_6$. Vanadium is V^{4+} and phosphorus is present as P^{5+}. Fourteen sulphurs possess a formal oxidation state of 1−, forming seven disulphide bonds $(S_2)^{2-}$ (six within the chains and the one $S_3PS–SPS_3$) and six sulphurs, three coordinated to each of the P^{5+} centres, of formal oxidation state 2−. A previous study showed that six Li^+ could be inserted into V_2PS_{10} giving a capacity of 355 mAh g^{-1}, for a single discharge-charge cycle. A large overpotential was observed during charging, and the mechanism of insertion was not studied as the intercalated structure was not investigated.[43]

Results and Discussion

Bulk V_2PS_{10} powder (Figure S2–S4) was synthesised from the elements in stoichiometric quantities as described in the Supporting Information. Small black needle-shaped crystals (Figure S5) of V_2PS_{10} were present in the powder which were selected for single crystal X-ray diffraction (SCXRD) (Table S1), and the structure of pristine V_2PS_{10} agrees well with that previously reported, shown in Figure 2c, e, and g. High sample purities of 98 wt% are achieved for V_2PS_{10} bulk powders (Tables S2–S5). For electrochemical tests, the as-made powder was further milled and sieved (Figure S6).

Electrochemical (de)insertion of Mg^{2+} was performed between 2.2 and 0.1 V vs. Mg^{2+}/Mg, in 0.5 M $Mg(TFSI)_2$/dimethoxyethane/1-methoxy-2-propylamine (3.84:1, w/w) (Figure S7, S9, Tables S6) with an OCV of 1.3 V vs. Mg^{2+}/Mg. A first-discharge capacity of 180 mAh g^{-1} (i.e., 1.6 Mg^{2+}/V_2PS_{10}) is obtained at a current density of 100 mA g^{-1}, yielding an average potential of 0.8 V (Figure 1a). After this initial discharge the capacity decreases to 100 mAh g^{-1} (i.e., 0.85 Mg^{2+}/V_2PS_{10}), which is maintained for the following 11 cycles with a capacity retention of 92%. The load curve for cycle 1 differs from subsequent cycles for which the potential profile remains similar; with plateaus at 1.3 V, 0.8 V, 0.6 V and 0.15 V in agreement with peak positions in cyclic voltammetry from cycle 2 onwards (Figure S10–S11). There is little change in the potential profile upon charging (Mg de-insertion) between cycle 1 and subsequent cycles. Plateaus observed above 2.0 V suggest some electrolyte decomposition is occurring, accounting for the larger capacity observed on charging. Above 2.0 V we are approaching the oxidative limit of the electrolyte (Figure S8), but remain within workable levels for cell investigations.[44] Approximately 2/3 of the capacity is obtained at 0.6 V, in early stages of the discharge process. The final 1/3 of the capacity is obtained between 0.6 V and 0.1 V, where a plateau is observed at 0.15 V. A range of current densities between 20–200 mA g^{1} were applied, yielding higher second cycle capacities (170 mAh g^{1} at 20 mA g^{-1} and 145 mAh g^{1} at 50 mA g^{1}, Figure 1b–c).

Magnesium insertion diffusion was studied by means of Potentiostatic Intermittent Titration Technique (PITT). Diffusion coefficients were calculated from the long-time region in which the current-time response follows the Cottrell behaviour to remove the effect of surface roughness; log(current) and time are proportional.[45] The diffusion

Angew. Chem. Int. Ed. **2024**, e202400837 (2 of 10)

© 2024 The Authors. Angewandte Chemie International Edition published by Wiley-VCH GmbH
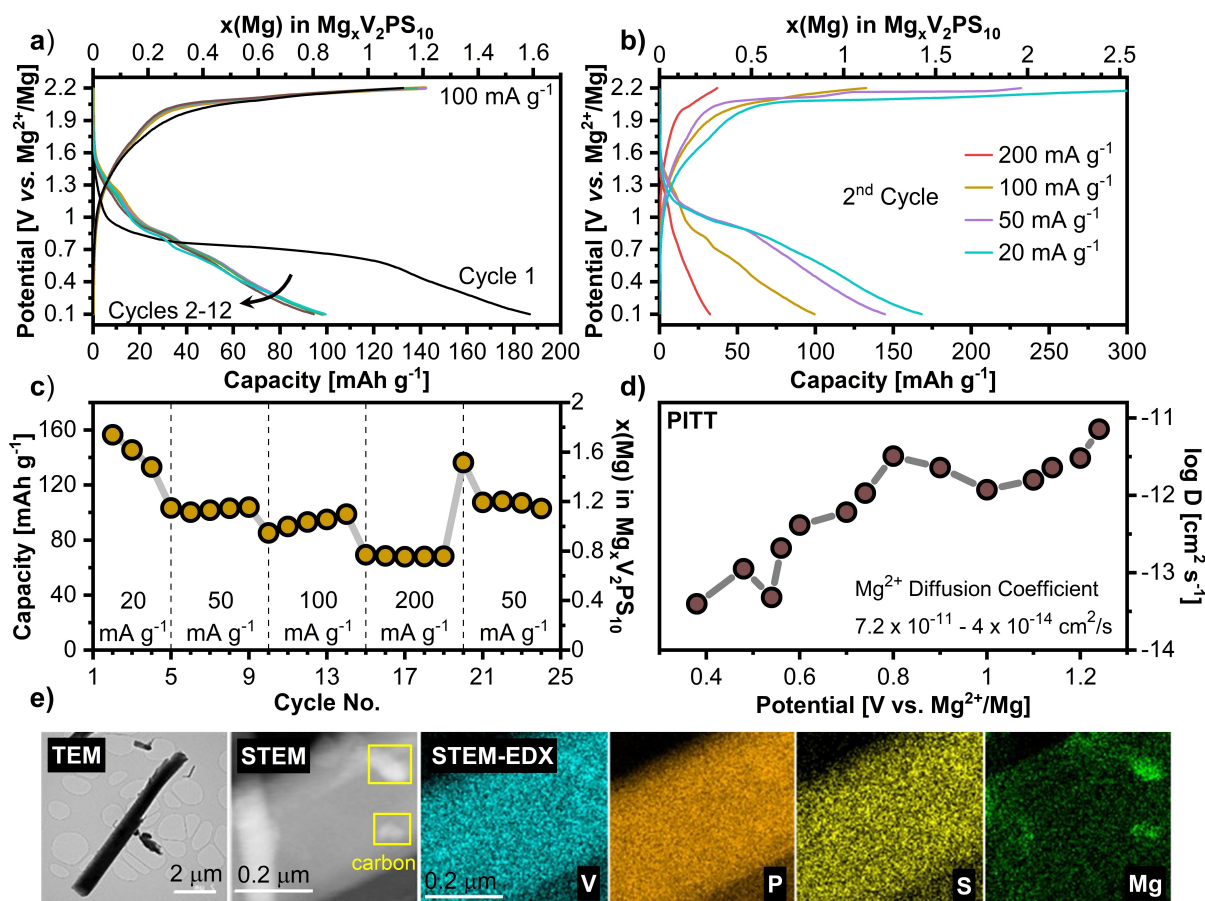
Figure 1. a) Voltage profiles of cycles 1–12 for V_2PS_{10} in 0.5 M $Mg(TFSI)_2$ in dimethoxyethane/1-methoxypropyl-2-amine (3.84/1, w/w) at 100 mA g^{-1}. **b)** Voltage profiles for V_2PS_{10} for cycle 2 at current densities of 200, 100, 50 and 20 mA g^{-1}. **c)** Rate performance of V_2PS_{10} for cycles 2–25 at current densities of 20, 50, 100 and 200 mA g^{-1}. **d)** Potentiostatic Intermittent Titration Technique of the discharge of V_2PS_{10} to calculate the Mg^{2+} diffusion coefficients as a function of potential. **e)** Electron microscope images of $Mg_{0.51}V_2PS_{10}$ after discharging to 0.1 V, left to right: TEM image of a $Mg_{0.51}V_2PS_{10}$ needle-like crystallite, STEM image of a section of a $Mg_{0.51}V_2PS_{10}$ crystallite, STEM-EDX false colour images of V, P, S and Mg content in $Mg_{0.51}V_2PS_{10}$. Magnesium- and carbon-containing species, from electrode preparation, on the surface of $Mg_{0.51}V_2PS_{10}$ particles are visible (Figure S13–14).

coefficients in $Mg_xV_2PS_{10}$ are $\approx 10^{-11}$–10^{-12} cm^2 s^{-1} above 0.8 V and show a continuous decrease to 4×10^{-14} cm^2 s^{-1} below 0.8 V towards the end of the discharge process (Figure 1d), indicating Mg-content dependent insertion kinetics. This range is similar to that observed for Mo_6S_8 (10^{-14}–10^{-11} cm^2 s^{-1} between 1.4–1.0 V).[46] Similarly to Li$^+$ insertion,[43] a large voltage hysteresis is observed between discharge and charge processes, which we believe is not due to mobility of the Mg in the material, but is inherent to the S–S bond breaking that form part of the observed redox processes. Though initial diffusion is relatively fast for Mg^{2+} (Figure 1d), the diffusion coefficient is three orders of magnitude lower at maximum magnesiation, so the observed hysteresis is a combination of these two effects. To understand the storage mechanism of V_2PS_{10}, Swagelok-type cells with cathodes consisting of approximately 20 mg powder of V_2PS_{10}/carbon black (60/40, w/w, no binder) were used to prepare samples of $Mg_xV_2PS_{10}$ for ex situ diffraction, X-ray photoelectron (XPS) and X-ray absorption (XAS) measurements. Typically, a second discharge capacity of 61 mAh g^{-1} (i.e., 0.51 Mg^{2+}/V_2PS_{10}) is achieved by 0.1 V (Figure S12).

Elemental analysis by STEM-EDX confirms the insertion of Mg^{2+} into bulk V_2PS_{10} (Figure 1e, S13, S14; Table S7, S8), yielding a Mg content of 0.4(2) Mg^{2+}/V_2PS_{10}, in close agreement with the expected Mg content from the measured capacity. Ex situ synchrotron X-ray diffraction (SXRD) analysis was performed on $Mg_xV_2PS_{10}$ ($0 \leq x \leq 0.51$) prepared at various potentials during discharge: 0.8 V ($x=0.17$); 0.6 V ($x=0.28$); 0.4 V ($x=0.35$); 0.2 V ($x=0.41$), 0.1 V ($x=0.51$); and recharging to 2.2 V ($x=0.00$).

Analysis of SXRD data for $Mg_{0.51}V_2PS_{10}$ (discharged to 0.1 V vs. Mg^{2+}/Mg) indicates the structural symmetry ($P2_1/c$) and framework of V_2PS_{10} is retained for cycled $Mg_xV_2PS_{10}$. Fourier difference analysis reveals three separate regions of electron density as suitable positions for Mg^{2+} within the unit cell (Figure S15–S16). Magnesium was placed on each of these three sites in turn, with an initial site occupancy of 0.5 (equating to $Mg_{0.75}V_2PS_{10}$) before refining atomic positions followed by occupancies. The proximity of Mg sites to V, P and S was restrained using a penalty function during final refinement, and the B_{iso} value for each Mg site was constrained to be equal. The refined occupancies of the

Angew. Chem. Int. Ed. **2024**, e202400837 (3 of 10)

© 2024 The Authors. Angewandte Chemie International Edition published by Wiley-VCH GmbH

three Mg sites in $Mg_{0.51}V_2PS_{10}$ were 0.425(16), 0.252(15) and 0.188(13), giving a total of 0.43(2) Mg^{2+}/V_2PS_{10}, in good agreement with the above-discussed electrochemical and elemental analysis data. Identification of discrete Mg insertion sites by modelling against bulk SXRD data confirms homogeneous distribution of Mg; exclusion of any one of these sites from the Rietveld model decreases the quality of the fit to the experimental data. Additionally, Raman spectroscopy shows no indication of the formation of nano-scale or amorphous species or elemental sulphur (Figure S17), suggesting that $Mg_xV_2PS_{10}$ $(0 \leq x \leq 0.51)$ operates via an insertion mechanism between OCV and 0.1 V vs. Mg^{2+}/Mg.

All three Mg sites are tetrahedrally coordinated by S^{2-} or S^{1-} (Figure 2f, h), with an average Mg–S bond length of 2.5(3) Å (range of 2.04–2.91 Å) and an average tetrahedral volume of 6.2(6) Å^3 (Figure S18–S19; Table S9, S10). Sulphide materials containing tetrahedrally coordinated MgS_4 units involving S^{2-} only, such as $Mg_2Mo_6S_6$,[23] $MgCr_2S_4$[47] and $MgAl_2S_4$,[48] have average Mg–S distances of 2.39(16) Å and average tetrahedral volumes of 6.5(6) Å^3.

Location of the three refined Mg positions is further confirmed by maximum entropy method (MEM), which generates the electron density distribution ab initio from observed diffraction data.[49] Analysis was performed on both V_2PS_{10} and $Mg_{0.51}V_2PS_{10}$ to visualize the change in charge density upon reduction of the host structure, and the resulting MEM maps show distinct regions of electron density attributed to Mg in the same tetrahedral environments identified via Fourier difference analysis and confirmed by Rietveld refinement (Figure 3a).

Considering the structural motif $V_4P_2(S_2)^{2-}_7S^{2-}_6$, insertion of 0.51 Mg^{2+} into V_2PS_{10} would yield $Mg_{1.02}V_4^{4+}P_2^{5+}(S_2)^{2-}_6S^{2-}_8$ where one S–S bond is cleaved, reducing $(S_2)^{2-}$ to $2S^{2-}$. MEM analysis reveals a change in the electronic structure of the bridging S(15)–S(20) disulphide bond between PS_4 units (Figure 3b–c). At the midway point along the vector S(15)→S(20), the electron density is 0.50 e$^-$Å^{-3} in V_2PS_{10}, which decreases to 0.21 e$^-$Å^{-3} in $Mg_{0.51}V_2PS_{10}$, in which electron density is more localized on the sulphur positions (Figure S20). Refinement of the S(15) and S(20) atomic positions reveals that these sites shift significantly from their original positions during formation of $Mg_{0.51}V_2PS_{10}$. Typical disulphide distances range from ≈1.9–2.18 Å with an ideal bond length of 2.05 Å.[50–52] This S(15)–S(20) inter-atomic distance increases by 0.32 Å (15.2%) from 2.081(17) Å in V_2PS_{10} to 2.397(13) Å in $Mg_{0.51}V_2PS_{10}$ (Figure 2c–d, Table S11), suggesting that the bridging disulphide bond in the $[P_2S_8]$ bitetrahedral unit of V_2PS_{10} is broken as a result of Mg insertion. This reduces $(S_2)^{2-}$ to $2S^{2-}$ and creates space for Mg insertion sites between the columns of VS_8 polyhedra originally connected by the $S_3PS–SPS_3$ bond.

Mg(1) and Mg(2) occupy positions at each end of the cleaved S–S bond in the space between chains originally bridged via the $[P_2S_8]$ units. Mg(1) forms bonds to two separate reduced $S(15)^{2-}$ from two different bridging bitetrahedral $[P_2S_8]$ groups; as such two $(S_2)^{2-}$ bonds must be broken from two different $[P_2V_4S_{20}]_\infty$ chains to create this

site (Figure S18–S19). Mg(1) also coordinates to two S^{1-} from the V–S chains. Mg(2) is coordinated to a reduced $S(20)^{2-}$ that had previously been bonded to $S(15)^{2-}$; only one $(S_2)^{2-}$ bond is broken to create this site. Mg(2) also coordinates to two S^{1-} and a S^{2-} (coordinated to both V and P) from the V–S chains. Unlike Mg(1) or Mg(2), Mg(3) does not interact with either S(15) or S(20) species, as it is located within the vdW gap between the pairs of $[P_2V_4S_{20}]_\infty$ infinite chains that are connected by the $S_3PS–SPS_3$ bond in pristine V_2PS_{10}. Mg(3) shares one edge and one corner with a VS_8 polyhedron, forming bonds with three S^{1-} and one of the original S^{2-} bound to P i.e., the mean valence of sulphur coordinating Mg(3) is less negative than for sulphur coordinating Mg(1) or Mg(2).

The cleavage of the bridging S–S bond between P^{5+} is supported by a decrease in the P(1)–S(15) and P(2)–S(20) bond lengths of 0.025(15) Å and PS_4 tetrahedral volumes from 4.58 Å^3 to 4.39 Å^3 as a result of the increase in formal negative charge on S(15) and S(20) (Table S11–S13). The distance between P(1) and P(2) increases from 4.39(1) Å to 4.56(1) Å.

The structural model for $Mg_{0.51}V_2PS_{10}$ was used as a starting model for refinement against SXRD data for other ex situ samples (Figure S21, Tables S14–S19). Refinement of Mg site occupancies shows increasing Mg content in $Mg_xV_2PS_{10}$ for decreasing potentials. For all compositions, the site occupancies (Figure 4g) follow the trend of Mg(1) > Mg(2) > Mg(3). Mg(1) and Mg(2) are preferentially occupied through reduction of bridging $(S_2)^{2-}$ bonds forming S^{2-} that coordinate to these sites (favouring electron transfer from V to S to maximise the number of possible S^{2-} sites, with Mg(1) and Mg(2) both coordinated to two S^{1-} and two S^{2-}). Mg(3) is coordinated to three S^{1-} and only one S^{2-}, which does not need to be created by S redox, with the higher coordination to S^{1-} making this site less favourable than the other two. The interatomic distance between S(15) and S(20) increases from 2.081(17) Å in V_2PS_{10} to 2.21(4) Å in $Mg_{0.06(2)}V_2PS_{10}$ (0.8 V), and reaches a maximum at 2.40(3) Å in $Mg_{0.36(2)}V_2PS_{10}$ (0.4 V), suggesting that $S_3PS–SPS_3$ bond cleavage occurs early in the discharge process, before levelling off at potentials below 0.4 V, as seen in Figure 4f and S17 (Table S20, Figure S22). None of the Mg sites observed through ex situ structural analysis are fully occupied. It is likely that the higher capacities recorded for non-ex situ cells are a result of greater occupancy across all three magnesium sites due to the difference in cell preparation.

The other $(S_2)^{2-}$ bond lengths in $Mg_{0.51}V_2PS_{10}$, those that are coordinated to V, remain below 2.11(13) Å, with an average change of 0.5% and a maximum increase of 0.10 Å compared to V_2PS_{10} (Table S21), consistent with localised cleavage solely of the $S_3PS–SPS_3$ bonds upon Mg insertion. The inter-chain distances for the bridged layer and the vdW layer increase from 6.529(10) Å and 6.229(10) Å to a maximum of 6.76(4) Å and 6.60(11) Å, respectively, for $Mg_{0.35}V_2PS_{10}$ (0.4 V), before decreasing to 6.479(10) Å and 6.396 Å in $Mg_{0.51}V_2PS_{10}$ (0.1 V). There are only very minor changes observed in the vanadium sulphide framework over the course of discharge; no $[VS_8]$ polyhedron changes its
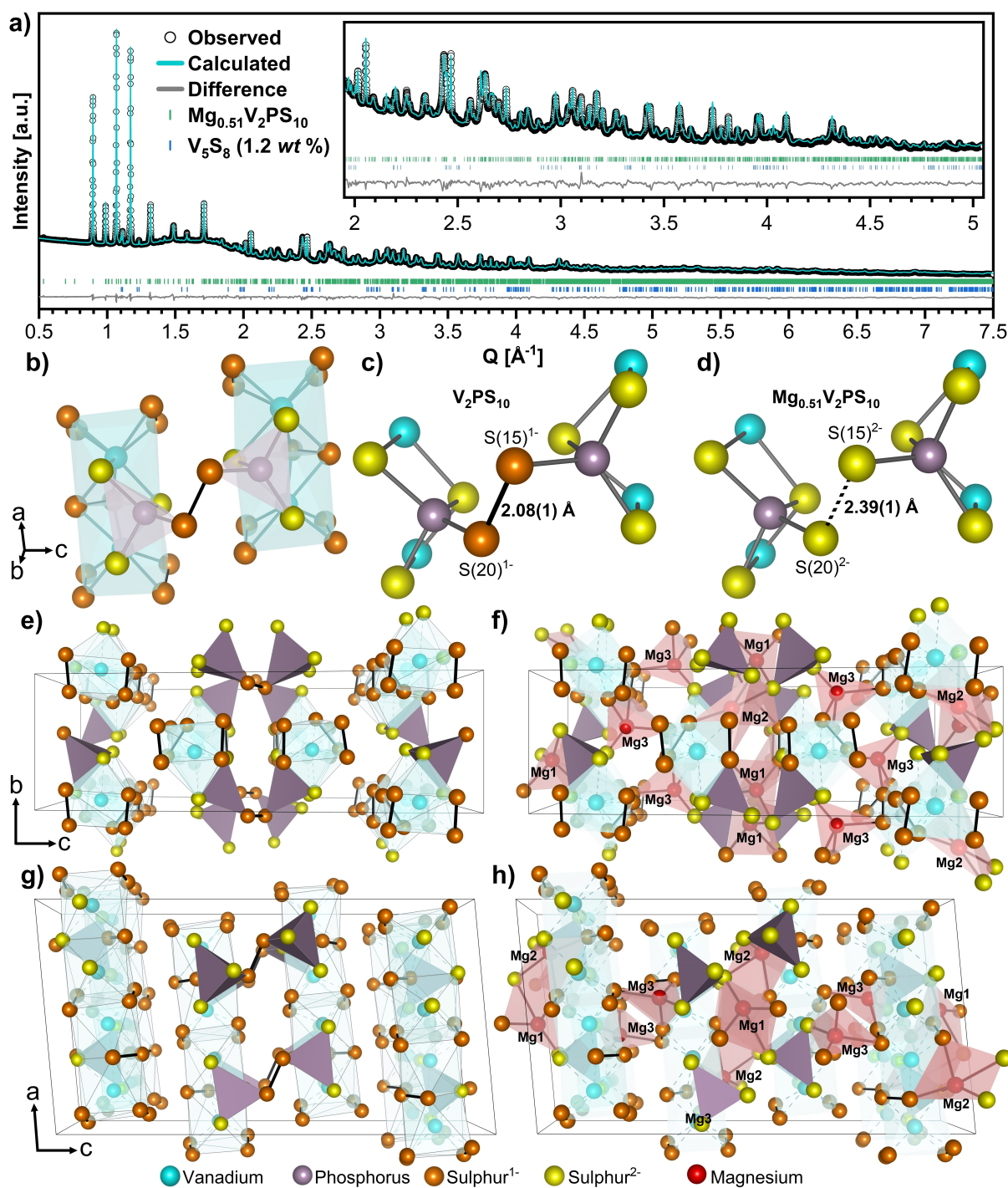
Figure 2. a) Rietveld refinement of SXRD data for $Mg_{0.51}V_2PS_{10}$ ($R_{wp} = 1.46\%$). **b)** V is coordinated to six S^{1-} (three $(S_2)^{2-}$ dimers) and two S^{2-} species in V_2PS_{10}. Successive V polyhedra share edges with PS_4 tetrahedra, with one P-bound S^{2-} bridging the two V centres. The polyhedra share faces to form $[P_2V_4S_{20}]_\infty$ chains parallel to the [100] direction. **c)–d)** Environment of the PS_4 tetrahedra in V_2PS_{10} and $Mg_{0.43(2)}V_2PS_{10}$, showing the increased distance between S(15) and S(20) upon Mg insertion. Unit cells of V_2PS_{10} and $Mg_{0.51}V_2PS_{10}$ projected along the **e)–f)** *a*-axes and **g)–h)** *b*-axes with vdW layers (empty in parent: location of Mg(3) in inserted material) and bridged layers (S_3PS–SPS_3 bond shown in parent; location of Mg(1) and Mg(2) between chains shown in inserted material where S–S bond is broken).

average V–S bond length, outside of error, for $0.0 \leq x \leq 0.51$; the overall average V–S bond length is 2.44(13) Å in V_2PS_{10}, 2.4(2) Å in $Mg_{0.36}V_2PS_{10}$ (0.4 V), and 2.44(14) Å in $Mg_{0.51}V_2PS_{10}$ (Table S22).

The strain induced upon insertion of Mg is absorbed by changes in inter-chain distances and cleavage of the S–S bond bridging the two PS_4 tetrahedra. As such, the unit cell volume of $Mg_{0.51}V_2PS_{10}$ increases only slightly (0.02 %) compared to V_2PS_{10}, from 2203.247(8) Å^3 to 2203.69(3) Å^3.
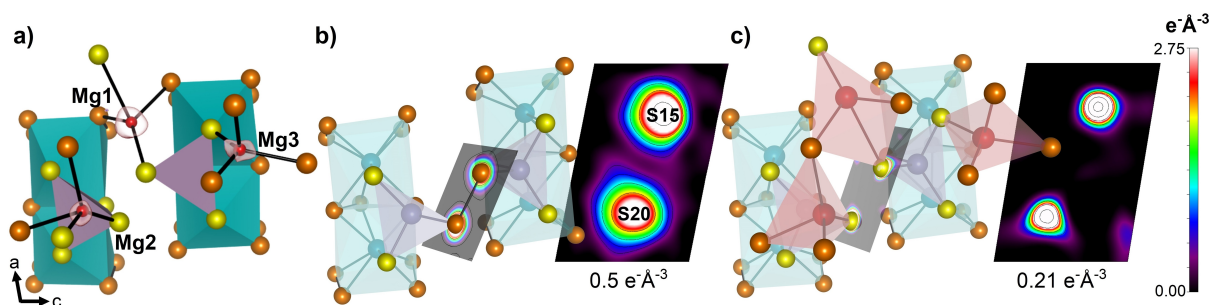
Figure 3. **a)** Electron density isosurfaces calculated from MEM for each of the three Mg sites present in $Mg_{0.51}V_2PS_{10}$ are shown in red. **b)–c)** 2D contour plots showing the electron density map of **b)** V_2PS_{10} and **c)** $Mg_{0.51}V_2PS_{10}$ along the S(15)−S(20) vector between the atoms forming the S−S bond that connects PS_4 units in V_2PS_{10}. The electron density quoted for each bond is determined from the voxel calculated as being at the midpoint of the vector S(15)→S(20).
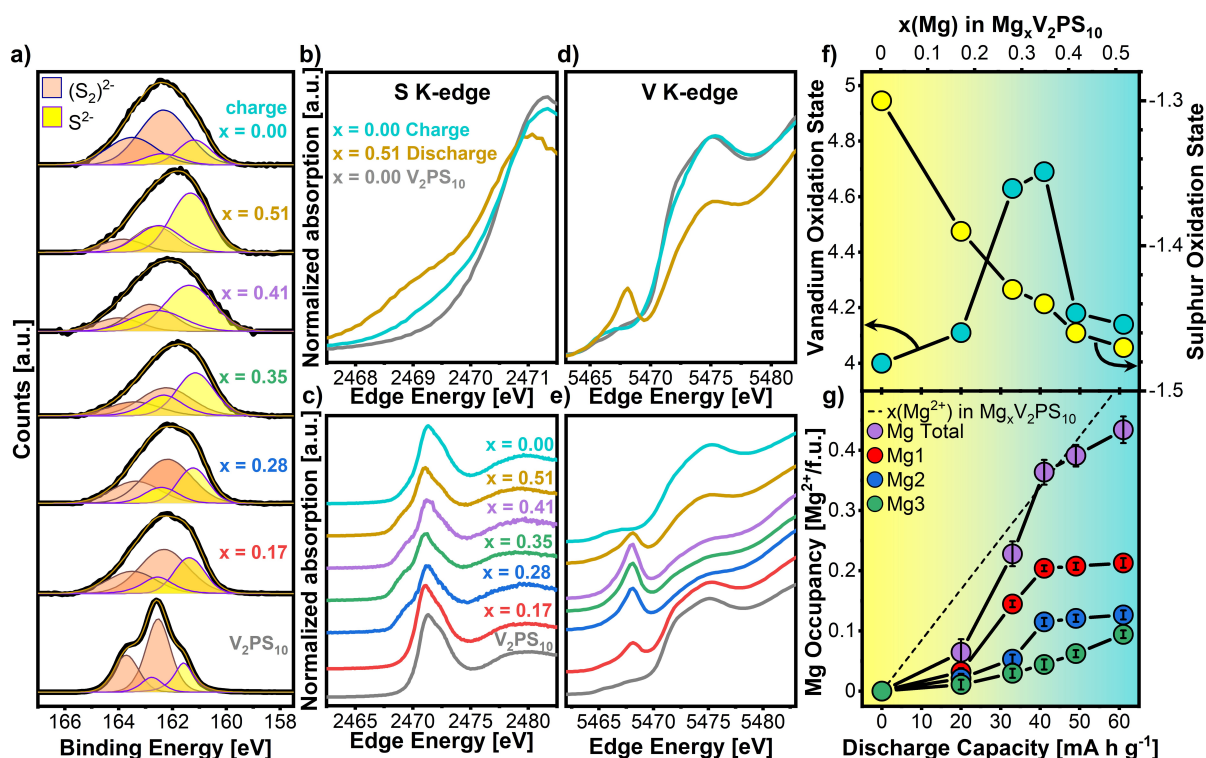

Figure 4. **a)** S 2p XPS spectra of $Mg_xV_2PS_{10}$ ($0 \leq x \leq 0.51$) at various states of discharge/charge. Both S 2p3/2 and S 2p1/2 contributions are shown for each sulphur species: $(S_2)^{2-}$ and S^{2-}. The sum of orbital contributions is shown as the gold envelope relative to the observed data (black line). **b)–e)**. Normalised S K-edge XANES data measured in fluorescence and V K-edge XANES data measured in transmission for $Mg_xV_2PS_{10}$. **b)** overlaid S K-edges for V_2PS_{10}, $Mg_{0.51}V_2PS_{10}$ (discharged to 0.1 V) and $Mg_xV_2PS_{10}$ ($x=0$) re-charged to 2.2 V; **c)** stacked S K-edges for $Mg_xV_2PS_{10}$. **d)** overlaid V K-edges for V_2PS_{10}, $Mg_{0.51}V_2PS_{10}$ (discharged to 0.1 V) and $Mg_xV_2PS_{10}$ ($x=0$) re-charged to 2.2 V showing a change in edge position; **e)** stacked V K-edges for $Mg_xV_2PS_{10}$. **f)–g)** Oxidation states of vanadium and sulphur and refined Mg site occupancies are given as a function of measured discharge capacity (bottom x-axis, in mAh g^{-1}), with corresponding expected Mg content (x(Mg) in $Mg_xV_2PS_{10}$ (top x-axis)). The yellow-blue background indicates the dominant redox mechanism at difference capacities of magnesium insertion. **f)** a plot of vanadium (left y-axis, blue dots) and sulphur (right y-axis, yellow dots) oxidation states taken from K-edge XAS by extrapolation from standard measurements of $V^{3+}_2O_3$, $V^{4+}_2O_4$, $V^{5+}_2O_5$ and FeS, FeS_2. **g)** Refined Mg(1), Mg(2), and Mg(3) and total Mg occupancies within $Mg_xV_2PS_{10}$ (per formula unit, considering Wyckoff position and site multiplicity within the unit cell). The expected Mg content from the measured electrochemical capacity is given by the dashed black line.

This increase is comparable with other zero-strain cathode materials reported in the literature, such as $Mg_xZr_2S_4$ ($0 \leq x \leq 1$) which displayed a 0.03% unit cell expansion for $x=0.7$.[53] The low volumetric strain observed upon insertion of magnesium in V_2PS_{10} may explain the fast diffusion kinetics observed for V_2PS_{10} (Figure 1c).

Upon re-charging from 0.1 to 2.2 V, refinement shows that magnesium is de-intercalated from $Mg_{0.51}V_2PS_{10}$, re-forming V_2PS_{10}. The total refined magnesium occupancy for

all states of discharge is in close agreement with the expected magnesium content calculated from the electrochemical capacity (Table S19). Additionally, the S(15)–S(20) distance decreases to 2.09(4) Å (within error of the starting material V_2PS_{10}) indicating that bond-cleavage is reversible, and the bridging S–S reforms upon removal of Mg^{2+}.

Spectroscopic methods were used to further examine the changes in electronic structure upon Mg insertion. S 2p X-ray photoelectron spectroscopy (XPS) measurements of V_2PS_{10} contains signals for both S^{2-} and $(S_2)^{2-}$ environments. Binding energies observed here are comparable to those observed for S^{2-} in PS_4-containing materials[54] and $(S_2)^{2-}$ in VS_4, $NaVS_4$ and K_3VS_4.[39] With increasing Mg content, the signal intensity of S^{2-} increases while that of $(S_2)^{2-}$ steadily decreases (Figure 4a). These observations support the analysis of SXRD data and indicate cleavage of $(S_2)^{2-}$ dimers within $Mg_xV_2PS_{10}$, and the resulting $(S_2)^{2-}/S^{2-}$ reduction during discharge. For all samples apart from V_2PS_{10}, there is a broadening of peak profiles and a shift to lower binding energies, suggesting that for any cycled sample a distribution of S redox states and S–V and S–P bond lengths exists. The reversibility of S–S cleavage, as indicated via ex situ diffraction analysis, is confirmed by the return of intensity to the $(S_2)^{2-}$ signal upon extraction of Mg. P^{5+} is confirmed to be redox inactive between 2.2–0.1 V (Figure S23).

X-ray Absorption Near-Edge Spectroscopy (XANES) measurements of S and V K-edges were used to monitor changes in oxidation state of bulk $Mg_xV_2PS_{10}$ at various stages of electrochemical cycling (Figure S24).[55] Reversible redox was observed on both the sulphur and vanadium sites from pristine V_2PS_{10} to fully discharged $Mg_{0.51}V_2PS_{10}$ (0.1 V), and to re-charged $Mg_0V_2PS_{10}$ (2.2 V).

There is a change in S oxidation state observed by XANES upon discharge, similar to the changes observed in sulphur 2p XPS measurements. S K-edge features arise from electronic excitations from the S 1s to S 3p/V 3d antibonding orbitals. As a result, S XANES gives information on the oxidation state of S.[39] The S edge decreases in energy from 2470.350 eV for V_2PS_{10} (average S oxidation of −1.3) to 2470.084 eV for $Mg_{0.22}V_2PS_{10}$ (formed at 0.4 V with an average S oxidation of −1.4); corresponding to the cleavage of one S–S bond, in agreement with structural analysis, confirming that S(15)–S(20) bond breakage occurs early in the discharge process. The S oxidation state is maintained at 2470.028 eV for $Mg_{0.51}V_2PS_{10}$ (Figure 4b–c). Upon charging, the edge profile and edge energy return to close to those of V_2PS_{10} (2470.280 eV), indicating that $2S^{2-}$ is oxidized to $(S_2)^{2-}$ and reversible anionic redox is achieved on the sulphur site.

The V K-edge XANES shows a shift in edge position from 5470.85 eV for V_2PS_{10} to 5472.15 eV for $Mg_{0.35}V_2PS_{10}$ (0.4 V). Additionally, over this same range a pre-edge peak forms at 5468.1 eV and increases in intensity, with increasing Mg content, relative to the height of the main absorption edge (Figure 4e–g). These observations are indicative of oxidation of V^{4+} towards V^{5+}, with the formation of the pre-edge feature indicative of dipole-forbidden 1 s to 3d electronic excitations resulting from changes in local symmetry, as observed for K_3VS_4 and Cu_3VS_4.[39,56–58] Further

discharge from $Mg_{0.41}V_2PS_{10}$ to $Mg_{0.51}V_2PS_{10}$ (0.2 V to 0.1 V) reverses the trend and results in V reduction from V^{5+} towards V^{4+}. This is observed by a shift in edge position from 5471.2 eV to 5471.1 eV and the concurrent decrease in intensity of the pre-edge feature.

The site occupancies at various discharge states are shown in Figure 4g, which agrees with the plateaus observed at different potentials during electrochemical cycling. By 0.4 V, insertion of 0.35 Mg^{2+} at sites Mg(1) and Mg(2) breaks the bridging S–S bonds between S(15) and S(20), reducing $(S_2)^{2-}$ to $2S^{2-}$ and oxidising V^{4+} towards V^{5+}.[40,59] This creates new S^{2-} that coordinate to intercalated magnesium at both sites, connecting the $[P_2V_4S_{20}]_\infty$ chains via new S–Mg–S bonds in place of the broken $S_3PS–SPS_3$ bond. Density functional theory (DFT) calculations probed the effect of Mg occupation of each of the three experimentally observed insertion sites. Separate models were created with a single Mg atom per experimental unit cell ($MgV_{16}P_8S_{80}$) at each of the three experimentally observed Mg sites, Mg(1), Mg(2) and Mg(3). This results in separate DFT models each with the composition $Mg_{0.125}V_2PS_{10}$ as well as pristine V_2PS_{10}. Figure 5a shows that both V 3d and S 3p states are present at the top of the valence band in pristine V_2PS_{10} (Figure S25).

The DFT optimised model for insertion of one Mg^{2+} onto one Mg(1) site in a unit cell, with composition of $Mg(1)_{0.125}V_2PS_{10}$, requires two $(S_2)^{2-}$ bonds being broken (Figure S26a, b), reducing two $(S_2)^{2-}$ to four S^{2-} anions. Isolated unoccupied V d states observed in the pDOS (Figure 5b), shown by the black circle, indicate an increase in the V oxidation state when Mg(1) site is occupied. This is confirmed by a decrease in magnetic moments for four V sites, consistent with V^{4+}/V^{5+} oxidation (Figure S27–30). This aligns with the experimentally observed V oxidation during early discharge despite the introduction of Mg (Figure 4). Extra electrons beyond the two per Mg are provided by creating the two $S(15)^{2-}$ anions through cleavage of two different S–S bonds per Mg(1) site. These electrons are transferred from V to S, creating the observed empty V 3d states in the gap.

The DFT optimised model for Mg(2) shows coordination to one reduced $S(15)^{2-}$ and one $S(20)^{2-}$ that originate from the same $S_3PS–SPS_3$ bond, in contrast to the redox-formed S^{2-} anions that coordinate to the Mg(1) site. Insertion onto the Mg(2) site requires only one $(S_2)^{2-}$ bond to be broken (Figure S26b), and therefore involves no transfer of electrons from V: the two electrons from Mg are sufficient. Accordingly, no isolated V d states are formed above the Fermi level (Figure 5d, S31–32), and there are no significant changes in the magnetic moments of the V states (Figure S32).

The Mg(3) site is located within the vdW layers between the originally $S_3PS–SPS_3$ connected double-chains of $V_4P_2S_{20}$ and away from the bridging S(15)–S(20) bonds that are broken when Mg(1) and Mg(2) are occupied. Insertion onto Mg(3) does not result in any S(15)–S(20) bond breaking in the DFT optimised model (Figure S33–34). Instead, charge compensation of Mg^{2+} insertion at Mg(3) is achieved by reduction of V as evidenced by two new occupied V d states
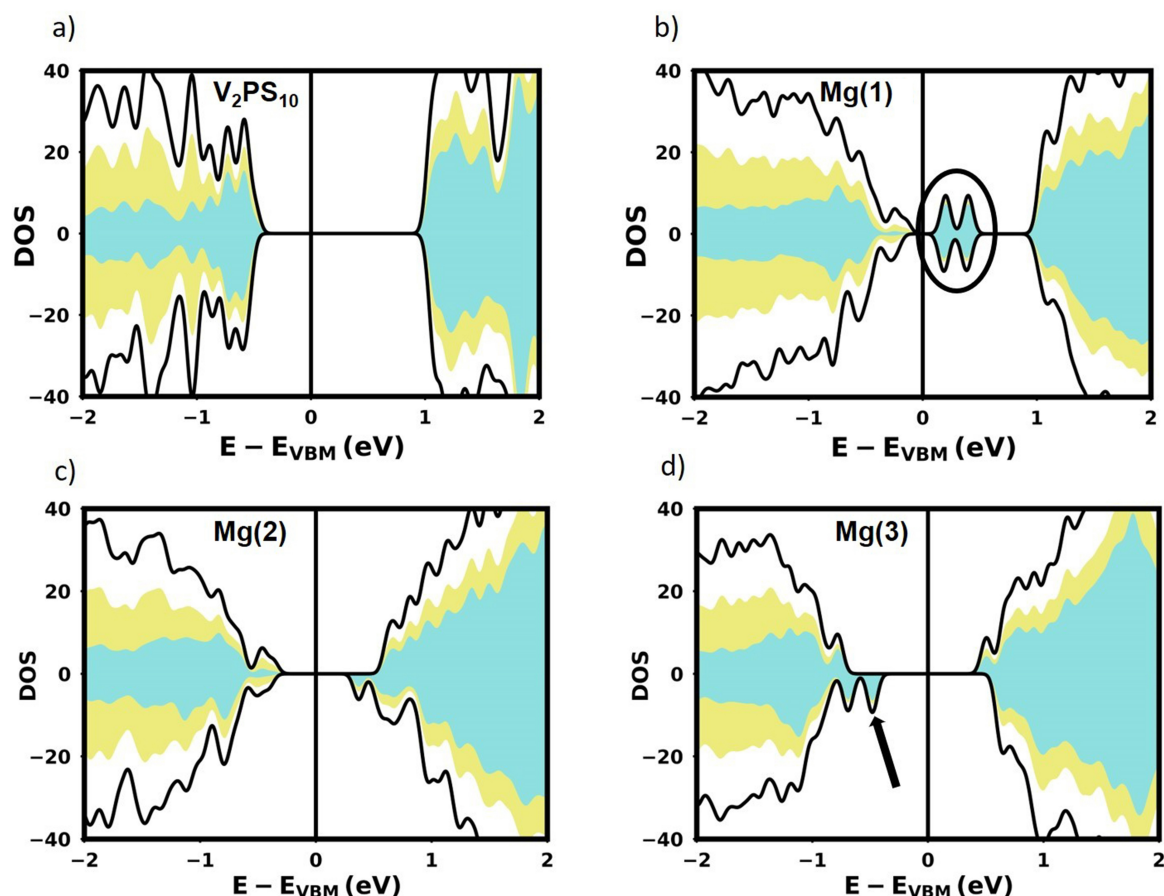
Figure 5. a) shows the projected density of states (pDOS) for V_2PS_{10}, with V 3d states shown in blue and sulfur 3p states shown in yellow. **b)** shows the pDOS for $Mg(1)_{0.125}V_2PS_{10}$ where one Mg is inserted into site Mg(1), showing empty isolated V d (black circle) states between the valence and conduction bands. **c)** shows the pDOS for $Mg(2)_{0.125}V_2PS_{10}$ where one Mg is inserted into site Mg(2) showing no isolated empty V d states. **d)** shows the pDOS for $Mg(3)_{0.125}V_2PS_{10}$ where one Mg is inserted into site Mg(3), showing the formation of new occupied V d states (black arrow) in the valence band.

between the valence and conduction bands (Figure 5d, black arrow) and an increase in the magnetic moments of two of the V (Figure S35). In common with the other two sites in the DFT calculations, and aligned with the experimentally refined structures, there is no breaking of the S–S bonds in the $(S_2)^{2-}$ anions that are coordinated to V, suggesting that cleavage of the chain-bridging $S_3PS–SPS_3$ bond is energetically more favourable than cleavage of the $(S_2)^{2-}$ bonds within the $[VS_8]$ chains.

These results align with experimentally observed XANES data (Figure 4f, g) in which the introduction of Mg(1) and Mg(2) by S reduction drives V oxidation to maximise S^{2-} bonding to the introduced Mg in a synergic way. Insertion of Mg(3) in the vdW layer involves re-reduction of vanadium from V^{5+} to V^{4+}, without breaking any S–S bonds, but resupplying to V the electrons originally used to break S–S bonds to create the Mg(1) site early in the insertion process. Overall, oxidation of V upon insertion into the Mg(1) site is counter-balanced by reduction of V upon insertion onto the Mg(3) site, resulting in a final V oxidation state of $+4.1$, very close to that of V_2PS_{10} ($+4.0$). This is consistent with the minimal structural perturbation

and lattice strain, as well as the fast kinetics of Mg^{2+} insertion.

Conclusion

V_2PS_{10} is a cathode for rechargeable magnesium batteries capable of reversible insertion of Mg^{2+}, with a capacity of $100\ mAh\,g^{-1}$ maintained for 10 cycles at $100\ mA\,g^{-1}$. It displays fast diffusion kinetics at the initial stages of Mg^{2+} insertion that are comparable with state-of-the-art Mo_6S_8, and is a zero-strain cathode over this potential and capacity range.

Detailed structural characterisation by SXRD and MEM demonstrate an insertion-type mechanism involving occupation of three separate Mg sites within $Mg_xV_2PS_{10}$. A mechanistic investigation by XANES and DFT calculations reveals the synergic involvement of anionic and cationic redox centres over the course of electrochemical cycling. The Mg coordination chemistry at each of the three insertion sites controls the nature of the species (anion or cation) involved in the electron transfer. In the early stages

of discharge, two Mg^{2+} insertion sites are created between chains of V_2PS_{10} by reversible reduction of bridging $(S_2)^{2-}$ bonds that are spatially separate from V, facilitated by additional electron transfer from V to break sufficient bonds to create the required S^{2-}-based coordination environments for Mg^{2+}. In later stages of discharge, below 0.4 V, further Mg^{2+} insertion onto a third site that occupies space between the vdW layers does not drive S–S bond breaking, and transfers electrons back to those V sites that were oxidised earlier in the insertion process, reducing V^{5+} to V^{4+}.

Mg^{2+} insertion results in redox both at the V metal centres and through cleavage of the $(S_2)^{2-}$ units that bridge separate chains of V_2PS_{10}, rather than those within the chains. This creates synergy between the occupancy of specific Mg sites, their sulphur coordination and the spatial location of the electrons that they transfer to the host. Spatial separation of the cationic and bond-specific anionic redox enables V_2PS_{10} to operate purely via an insertion process, unlike VS_4 and TiS_3, demonstrating a cooperative mechanism that enables reversible electrochemical redox behaviour. Bond-specific anion redox may be considered in materials design of future positive electrode materials for Mg-cells.[26]

Supporting Information

All underlying data will be published at https://datacat.liverpool.ac.uk/id/eprint/2568. Deposition Number(s) https://www.ccdc.cam.ac.uk/services/structures?id=doi:10.1002/anie.20230XXX2324151 (for pristine V_2PS_{10}), 2324150 (for $Mg_{0.51}V_2PS_{10}$ after cycling to a voltage of 0.1 V) contain the supplementary crystallographic data for this paper. These data are provided free of charge by the joint Cambridge Crystallographic Data Centre and Fachinformationszentrum Karlsruhe http://www.ccdc.cam.ac.uk/structures.

Conflict of Interest

The authors declare no conflict of interest.

Data Availability Statement

The data that support the findings of this study are openly available in University of Liverpool Data Repository at https://datacat.liverpool.ac.uk/id/eprint/2568, reference number 2568.

[1] M. Armand, J. M. Tarascon, *Nature* **2001**, *414*, 359–367.
[2] M. Mao, T. Gao, S. Hou, C. Wang, *Chem. Soc. Rev.* **2018**, *47*, 8804–8841.
[3] W. M. Haynes, *CRC Handbook of Chemistry and Physics*, CRC Press, **2011**.
[4] P. Atkins, T. Overton, J. Rourke, M. Weller, F. Armstrong, M. Hagerman, *Inorganic Chemistry*, W. H. Freeman, **2010**.
[5] H. D. Yoo, I. Shterenberg, Y. Gofer, G. Gershinsky, N. Pour, D. Aurbach, *Energy Environ. Sci.* **2013**, *6*, 2265–2279.
[6] J. Heelan, E. Gratz, Z. Zheng, Q. Wang, M. Chen, D. Apelian, Y. Wang, *JOM* **2016**, *68*, 2632–2638.
[7] R. Davidson, A. Verma, D. Santos, F. Hao, C. Fincher, S. Xiang, J. Van Buskirk, K. Xie, M. Pharr, P. P. Mukherjee, S. Banerjee, *ACS Energy Lett.* **2019**, *4*, 375–376.
[8] E. Levi, Y. Gofer, D. Aurbach, *Chem. Mater.* **2010**, *22*, 860–868.
[9] C. Ling, D. Banerjee, M. Matsui, *Electrochim. Acta* **2012**, *76*, 270–274.
[10] Z. Guo, S. Zhao, T. Li, D. Su, S. Guo, G. Wang, *Adv. Energy Mater.* **2020**, 1903591.
[11] R. D. Shannon, *Acta Crystallogr.* **1976**, *A32*, 751–767.
[12] C. Drosos, C. Jia, S. Mathew, R. G. Palgrave, B. Moss, A. Kafizas, D. Vernardou, *J. Power Sources* **2018**, *384*, 355–359.
[13] C. Ling, F. Mizuno, *Chem. Mater.* **2013**, *25*, 3062–3071.
[14] R. E. Doe, T. K. Mueller, G. Ceder, J. Barker, K. A. Persson, *Electrode Materials for Magnesium Batteries*, **2012**, U. S.Patent US20120219859 A1.
[15] J. Wu, G. Gao, G. Wu, B. Liu, H. Yang, X. Zhou, J. Wang, *RSC Adv.* **2014**, *4*, 15014–15017.
[16] J. W. Choi, D. Aurbach, *Nat. Rev. Mater.* **2016**, *1*, 1–16.
[17] Z. Ma, D. R. MacFarlane, M. Kar, *Batteries & Supercaps* **2019**, *2*, 115–127.
[18] Y. Liang, R. Feng, S. Yang, H. Ma, J. Liang, J. Chen, *Adv. Mater.* **2011**, *23*, 640–643.
[19] X. Sun, P. Bonnick, V. Duffort, M. Liu, Z. Rong, K. A. Persson, G. Ceder, L. F. Nazar, *Energy Environ. Sci.* **2016**, *9*, 2273–2277.
[20] M. Liu, A. Jain, Z. Rong, X. Qu, P. Canepa, R. Malik, G. Ceder, K. A. Persson, *Energy Environ. Sci.* **2016**, *9*, 3201–3209.
[21] H. D. Yoo, Y. Liang, H. Dong, J. Lin, H. Wang, Y. Liu, L. Ma, T. Wu, Y. Li, Q. Ru, Y. Jing, Q. An, W. Zhou, J. Guo, J. Lu, S. T. Pantelides, X. Qian, Y. Yao, *Nat. Commun.* **2017**, *8*, 339.
[22] X. Sun, P. Bonnick, L. F. Nazar, *ACS Energy Lett.* **2016**, *1*, 297–301.
[23] D. Aurbach, Z. Lu, A. Schechter, Y. Gofer, H. Gizbar, R. Turgeman, Y. Cohen, M. Moshkovich, E. Levi, *Nature* **2000**, *407*, 724–727.
[24] V. Duffort, X. Sun, L. F. Nazar, *Chem. Commun.* **2016**, *52*, 12458–12461.

[25] A. Débart, L. Dupont, R. Patrice, J.-M. Tarascon, *Solid State Sci.* **2006**, *8*, 640–651.

[26] A. M. Abakumov, S. S. Fedotov, E. V. Antipov, J.-M. Tarascon, *Nat. Commun.* **2020**, *11*, 4976.

[27] Y. Cao, Y. Zhu, C. Du, X. Yang, T. Xia, X. Ma, C. Cao, *ACS Nano* **2022**, *16*, 1578–1588.

[28] M. Mao, X. Ji, S. Hou, T. Gao, F. Wang, L. Chen, X. Fan, J. Chen, J. Ma, C. Wang, *Chem. Mater.* **2019**, *31*, 3183–3191.

[29] S. Y. Kim, C. S. Park, S. Hosseini, J. Lampert, Y. J. Kim, L. F. Nazar, *Adv. Energy Mater.* **2021**, *11*, 2100552.

[30] G. Assat, D. Foix, C. Delacourt, A. Iadecola, R. Dedryvère, J.-M. Tarascon, *Nat. Commun.* **2017**, *8*, 2219.

[31] K. Luo, M. R. Roberts, N. Guerrini, N. Tapia-Ruiz, R. Hao, F. Massel, D. M. Pickup, S. Ramos, Y.-S. Liu, J. Guo, A. V. Chadwick, L. C. Duda, P. G. Bruce, *J. Am. Chem. Soc.* **2016**, *138*, 11211–11218.

[32] N. Yabuuchi, M. Takeuchi, M. Nakayama, H. Shiiba, M. Ogawa, K. Nakayama, T. Ohta, D. Endo, T. Ozaki, T. Inamasu, K. Sato, S. Komaba, *Proc. Nat. Acad. Sci.* **2015**, *112*, 7650–7655.

[33] I. D. Johnson, B. J. Ingram, J. Cabana, *ACS Energy Lett.* **2021**, *6*, 1892–1900.

[34] B. Li, D. Xia, *Adv. Mater.* **2017**, *29*, 1701054.

[35] S. Britto, M. Leskes, X. Hua, C.-A. Hébert, H. S. Shin, S. Clarke, O. Borkiewicz, K. W. Chapman, R. Seshadri, J. Cho, C. P. Grey, *J. Am. Chem. Soc.* **2015**, *137*, 8499–8508.

[36] K. Taniguchi, Y. Gu, Y. Katsura, T. Yoshino, H. Takagi, *Appl. Phys. Express* **2016**, *9*, 11801.

[37] Y. Wang, Z. Liu, C. Wang, X. Yi, R. Chen, L. Ma, Y. Hu, G. Zhu, T. Chen, Z. Tie, J. Ma, J. Liu, Z. Jin, *Adv. Mater.* **2018**, *30*, 1802563.

[38] M. Arsentev, A. Missyul, A. V. Petrov, M. Hammouri, *J. Phys. Chem. C* **2017**, *121*, 15509–15515.

[39] S. Dey, J. Lee, S. Britto, J. M. Stratford, E. N. Keyzer, M. T. Dunstan, G. Cibin, S. J. Cassidy, M. Elgaml, C. P. Grey, *J. Am. Chem. Soc.* **2020**, *142*, 19588–19601.

[40] Z. Li, B. P. Vinayan, P. Jankowski, C. Njel, A. Roy, T. Vegge, J. Maibach, J. M. G. Lastra, M. Fichtner, Z. Zhao-Karger, *Angew. Chem. Int. Ed.* **2020**, *59*, 11483–11490.

[41] V. Bodenez, L. Dupont, M. Morcrette, C. Surcin, D. W. Murphy, J.-M. Tarascon, *Chem. Mater.* **2006**, *18*, 4278–4287.

[42] R. Brec, G. Ouvrard, M. Evain, P. Grenouilleau, J. Rouxel, *J. Solid State Chem.* **1983**, *47*, 174–184.

[43] R. Brec, G. Ouvrard, *Solid State Ionics* **1983**, *9–10*, 481–484.

[44] S. Hou, X. Ji, K. Gaskell, P.-F. Wang, L. Wang, J. Xu, R. Sun, O. Borodin, C. Wang, *Science* **2021**, *374*, 172–178.

[45] M. D. Levi, D. Aurbach, *J. Phys. Chem. B* **1997**, *101*, 4641–4647.

[46] E. Lancry, E. Levi, Y. Gofer, M. D. Levi, D. Aurbach, *J. Solid State Electrochem.* **2005**, *9*, 259–266.

[47] A. Wustrow, B. Key, P. J. Phillips, N. Sa, A. S. Lipton, R. F. Klie, J. T. Vaughey, K. R. Poeppelmeier, *Inorg. Chem.* **2018**, *57*, 8634–8638.

[48] R. C. Sharma, Y. A. Chang, *J. Phase Equilib.* **1987**, *8*, 128–131.

[49] S. van Smaalen, L. Palatinus, M. Schneider, *Acta Crystallogr. Sect. A* **2003**, *59*, 459–469.

[50] H. Fukuoka, N. Kawata, M. Furuta, Y. Katakami, S. Kimura, K. Inumaru, *Inorg. Chem.* **2020**, *59*, 13320–13325.

[51] N. E. Brese, M. O'Keeffe, *Acta Crystallogr. Sect. B* **1991**, *47*, 192–197.

[52] D. I. Brown, *J. Mater. Sci.* **2017**, *52*, 9959–9962.

[53] P. Bonnick, L. Blanc, S. H. Vajargah, C.-W. Lee, X. Sun, M. Balasubramanian, L. F. Nazar, *Chem. Mater.* **2018**, *30*, 4683–4693.

[54] C. Dietrich, R. Koerver, M. W. Gaultois, G. Kieslich, G. Cibin, J. Janek, W. G. Zeier, *Phys. Chem. Chem. Phys.* **2018**, *20*, 20088–20095.

[55] B. Ravel, M. Newville, *J. Synchrotron Radiat.* **2005**, *12*, 537–541.

[56] J. Wong, F. W. Lytle, R. P. Messmer, D. H. Maylotte, *Phys. Rev. B* **1984**, *30*, 5596–5610.

[57] S. R. Sutton, J. Karner, J. Papike, J. S. Delaney, C. Shearer, M. Newville, P. Eng, M. Rivers, M. D. Dyar, *Geochim. Cosmochim. Acta* **2005**, *69*, 2333–2348.

[58] D. A. McKeown, I. S. Muller, K. S. Matlack, I. L. Pegg, *J. Non-Cryst. Solids* **2002**, *298*, 160–175.

[59] Z. Li, J. Häcker, M. Fichtner, Z. Zhao-Karger, *Adv. Energy Mater.* **2023**, *13*, 2300682.
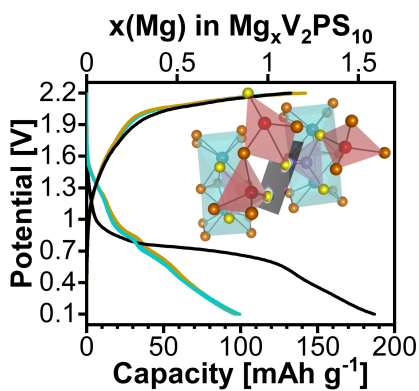
Research Articles

Batteries

M. A. Wright, T. W. Surta, J. A. Evans, J. Lim,
H. Jo, C. J. Hawkins, M. Bahri,
L. M. Daniels, R. Chen, M. Zanella,
L. G. Chagas, J. Cookson, P. Collier,
G. Cibin, A. V. Chadwick, M. S. Dyer,
N. D. Browning, J. B. Claridge,
L. J. Hardwick,
M. J. Rosseinsky* ———— e202400837

Accessing Mg-Ion Storage in V_2PS_{10} via Combined Cationic-Anionic Redox with Selective Bond Cleavage

V_2PS_{10} achieves reversible capacity of 100 mAh g^{-1} with fast Mg^{2+} insertion kinetics. Insertion is accompanied by simultaneous anionic and cationic redox on spatially separated sites. The nature of the electron transfer depends on the coordination of individual Mg sites by the distinct sulphur species involved, creating synergy between specific site occupancies and the selective cleavage of one of the two chemically distinct sets of S—S bonds.